Journal of Alloys and Compounds xxx (xxxx) xxx

Contents lists available at ScienceDirect

Journal of Alloys and Compounds

journal homepage: http://www.elsevier.com/locate/jalcom

The role of Al^{+3} on the microstructural and electrical properties of $Na_{1+x}Al_xTi_{2-x}(PO_4)_3$ NASICON glass-ceramics

Adriana M. Nieto-Muñoz [a, *], Jairo F. Ortiz-Mosquera [a], Ana C.M. Rodrigues [b]

[a] Programa de Pós-graduação em Ciência e Engenharia de Materiais, Universidade Federal de São Carlos, CP 676, 13565-905, São Carlos, SP, Brazil
[b] Departamento de Engenharia de Materiais, Universidade Federal de São Carlos, CP 676, 13565-905, São Carlos, SP, Brazil

ARTICLE INFO

Article history:
Received 12 August 2019
Received in revised form
21 November 2019
Accepted 22 November 2019
Available online xxx

Keywords:
NASICON
Solid electrolyte
Sodium-ion conductor
Glass-ceramics
Electrical modulus
Grain boundary

ABSTRACT

Sodium-ion conducting glass-ceramics are synthesized by crystallization of $Na_{1+x}Al_xTi_{2-x}(PO_4)_3$ ($0 \leq x \leq 1.4$) (NATP) parent glasses. The thermal characterization of glasses is performed by Differential Scanning Calorimetry (DSC) and allowed to determine the glass transition (T_g) and crystallization (T_x) temperatures. An increase in the T_x - T_g parameter is observed, indicating that the thermal stability of glasses against crystallization and also the glass-forming ability increase with the inclusion of Al_2O_3. The X-ray results show that the $NaTi_2(PO_4)_3$ phase is the majority phase after the crystallization of the precursor glasses at T_x/ 30 min. X-ray results also confirm that the limit of solid solution is reached for $x = 1.0$. Electrical measurements indicate that the addition of aluminum ions promotes a decrease in activation energy resulting in the increment of the total ionic conductivity of glass-ceramics by up to five orders of magnitude when compared to the free-aluminum sample. The best sodium-conductive glass-ceramic is obtained for $x = 1.0$ with a total ionic conductivity of 3.2×10^{-3} S cm^{-1} at 300 °C and activation energy of 0.47 eV. Using the impedance data converted to the electric modulus formalism, the contribution of the grain and grain boundary in total ionic conductivity is analyzed. Finally, an increase in the average grain size of the glass-ceramics with the addition of aluminum is also observed, which contributes to the enhancement of overall ionic conductivity.

1. Introduction

The growing demand for alternative energy sources has raised interest in the development of renewable and inexpensive storage devices, such as sodium-based ones because of abundant availability, low production cost and low toxicity of sodium [1–4]. Different materials have been investigated to improve the operation of sodium-ion batteries in relation to operating temperatures and power generation. Thus, materials with a NASICON-type (Na Super Ionic Conductor) $AM_2(PO_4)_3$ structure, where A is a monovalent cation (Li^+, Na^+, K^+) and M is a tetravalent cation (Ti^{+4}, Ge^{+4}, Zr^{+4}, Sn^{+4}), are considered good candidates for application as solid electrolytes in sodium batteries due to their high ionic conductivity [5,6]. The NASICON structure is described as a network with three-dimensional channels formed by the arrangement of MO_6 octahedra linked by corners to PO_4 tetrahedra that allow the movement of charge carrier ions "A" through the structure. It is known that high conductivities (from 10^{-4} to 10^{-2} S cm^{-1} at operating temperatures) are reached in NASICON materials by aliovalent substitutions with ions of lower valences on M − and/or P-sites. It is also known that these substitutions promote the increase in the concentration of charge carriers to compensate the excess of negative charges, consequently leading to an increase in ionic conductivity [6–8].

$Li_{1+x}Al_xTi_{2-x}(PO_4)_3$ (LATP) series is one of the most interesting NASICON compounds, since this family exhibits the highest values of conductivity among lithium ion-conducting systems, reaching 1.3×10^{-3} S cm^{-1} for $x = 0.3$ at room temperature [7]. There is a vast body of literature on attempts to improve the properties of this system, either by analyzing conduction phenomena, the influence of synthesis routes, or microstructure variation due to the inclusion of different elements. [4,6,9]. Although these compounds exhibit high Li^+ ionic conductivity, there are very few studies on the sodium-containing analogous series, $Na_{1+x}Al_xTi_{2-x}(PO_4)_3$ (NATP). One of the few studies on this NASICON series was carried out by Mouahid et al. [10]. The authors obtained NATP ceramics with different amounts of aluminum ($0.4 \leq x \leq 0.9$) by solid-state

* Corresponding author.
E-mail address: adriana.nieto@ppgcem.ufscar.br (A.M. Nieto-Muñoz).

https://doi.org/10.1016/j.jallcom.2019.153148
0925-8388/

reaction. In their work, it is mentioned that the increase in aluminum content favors ionic conductivity because the number of charge carriers is also increased. However, the authors obtained samples with a porosity of up to 25%. It is known that microstructure factors, such as porosity and grain boundary characteristics, may decrease the electrical conductivity of the compound, affecting its use as a solid electrolyte. An alternative to reduce the porosity and optimize the ionic conductivity is to synthesize the NATP series by the glass-ceramic route, which consists of the controlled crystallization of a precursor glass. In fact, several studies show that glass-ceramics exhibit low porosity and their microstructure can be also controlled by different crystallization treatments of the precursor glass [11,12].

Thus, this article focuses on evaluating the effect of aluminum concentration on the structural, microstructural and electrical properties of the $Na_{1+x}Al_xTi_{2-x}(PO_4)_3$ system ($0 \leq x \leq 1.4$) obtained via glass-ceramic route. Note that this is a larger composition range than that investigated by Mouhaid et al. [10]. The structural and microstructural evolution of glass-ceramics with aluminum content was analyzed by X-ray diffraction and scanning electron microscopy (SEM), respectively. The ionic conductivity has been measured by impedance spectroscopy. Using different formalisms to treat the impedance data allowed the separation of grain and grain boundary contributions in the total conductivity of $Na_{1+x}Al_xTi_{2-x}(PO_4)_3$ glass ceramics, with $x = 0.0$, 0.4, 0.6 and 0.8.

2. Experimental procedure

2.1. Synthesis of precursor glasses

Precursor glasses of $Na_{1+x}Al_xTi_{2-x}(PO_4)_3$ ($0 \leq x \leq 1.4$) series were obtained by the melt-quenching method in 20 g batches. Sodium carbonate (Na_2CO_3, Vetec 99.9%), titanium dioxide (TiO_2, Aldrich > 99.9%), aluminum oxide (Al_2O_3, Aldrich 99,99%) and dihydroxy ammonium phosphate ($(NH_4)_2HPO_4$, Aldrich > 98%) were weighed and mixed in an appropriate proportion (see Table 1) in a rotary ball-mill for 12 h. After homogenization, the powders were heated to 400 °C and 700 °C for 4 h and 2 h, respectively, to promote the decomposition of the Na_2CO_3 and $(NH_4)_2HPO_4$ precursor materials. Subsequently, the mixture was heated up to 1450 °C and melted for 1 h. The resulting melt was poured and pressed between two aluminum plates to promote a fast cooling process and thus, the formation of vitreous material. All parent glasses were annealed at 40 °C below the glass transition temperature (T_g) for 2 h to release thermal stress and then cooled inside the furnace at a very slow cooling rate until room temperature.

2.2. Heat treatments of parent glasses and characterization techniques

The characteristic temperatures of the NATP precursor glasses (glass transition (T_g) and crystallization temperature (T_x)) were determined by differential scanning calorimetry (DSC) in an air atmosphere at a heating rate of 10 K/min. Posteriorly, the glass-ceramic samples were obtained by single heat treatment of precursor glasses at the onset of its corresponding crystallization temperature (T_x) for 30 min in a tubular electric furnace with a temperature accuracy of ±1 °C.

X-ray diffraction (XRD) was used to confirm the amorphous nature of glass samples and to determine the crystalline phases of glass-ceramics. The structural characterization was carried out using a Rigaku Ultima IV X-ray diffractometer and Cu K_α radiation in a 2θ range of 10° − 80°, scan step size of 0.02° and an integration time of 0.66 s. The indexing of the crystalline phases in X-ray patterns was performed using the Crystallographic Search-Match program database [13]. Posteriorly, the powder patterns were analyzed by Rietveld refinements using the TOPAS-Academic software version 6 [14] in combination with the Inorganic Crystal Structure Database (ICSD) [15].

Regarding the electrical characterization, both vitreous and glass-ceramic samples were analyzed by complex impedance spectroscopy using a Novocontrol Alpha Analyzer utilizing a two-point sample holder, in a frequency range of 10 MHz to 0.1 Hz and at a temperature range from 50 °C to 300 °C. All samples were previously cut in parallelepipedal shape of about 0.8 − 1.2 mm thickness, and area of 0.1 − 0.2 cm^2. These samples were polished, and then, gold electrodes were sputtered on their parallel sides.

Glass-ceramic microstructures were also observed by scanning electron microscopy (SEM- Phillips XL30 FEG) on the fracture surface with a beam voltage of 10 kV.

3. Results and discussion

3.1. Synthesis and thermal characterization of glasses by differential scanning calorimetry (DSC)

Except for the free-aluminum composition NATP00 or $x = 0.0$, vitreous precursor materials were obtained for all investigated compositions (See Table 1). In fact, the liquid corresponding to the NATP00 composition crystallized during cooling. For the NATP04 ($x = 0.4$) sample, the low viscosity liquid partially crystallized during cooling, allowing a small amount of precursor glass to be obtained. All precursor glasses were transparent and presented a purple tonality, as shown in Fig. 1. Narváez-Semanate et al. [9] and Chowdari et al. [16] also observed this purple color in glasses from the lithium-homologous series, $Li_{1+x}Al_xTi_{2-x}(PO_4)_3$. According to Narváez-Semanate, the purple tonality is due to the reduction of

Table 1
Nominal composition (mol %) of $Na_{1+x}Al_xTi_{2-x}(PO_4)_3$ parent glasses.

Sample name	x	Na_2O	Al_2O_3	TiO_2	P_2O_5
		(mol %)			
NATP00[a]	0.0	12.5	0.0	50.0	37.5
NATP04	0.4	17.5	5.0	40.0	37.5
NATP06	0.6	20.0	7.5	35.0	37.5
NATP08	0.8	22.5	10.0	30.0	37.5
NATP10	1.0	25.0	12.5	25.0	37.5
NATP12	1.2	27.5	15.0	20.0	37.5
NATP14	1.4	30.0	17.5	15.0	37.5

[a] Crystallized during cooling.

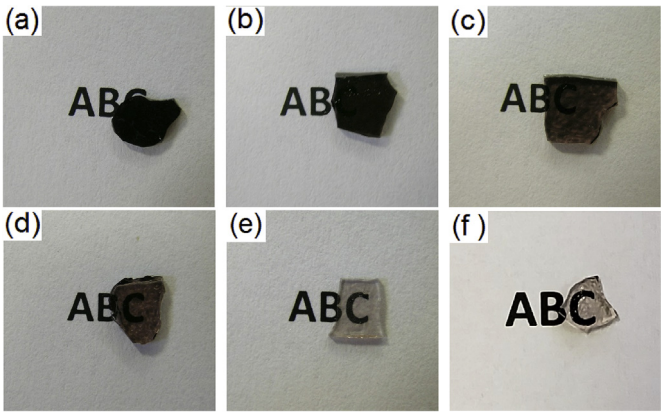

Fig. 1. Photographs of precursor glass samples with compositions (a) NATP04, (b) NATP06, (c) NATP08, (d) NATP10, (e) NATP12 and (f) NATP14.

Please cite this article as: A.M. Nieto-Muñoz et al., The role of Al^{+3} on the microstructural and electrical properties of $Na_{1+x}Al_xTi_{2-x}(PO_4)_3$ NASICON glass-ceramics, Journal of Alloys and Compounds, https://doi.org/10.1016/j.jallcom.2019.153148

Ti^{+4} to Ti^{+3} during glass melting. Chowdari attributed this behavior to the presence of ammonia, which could act as a reducing agent during the synthesis of glass. However, Narváez-Semanate et al. obtained a purple glass using P_2O_5 as a starting material, thus excluding the hypothesis proposed by Chowdari. Fig. 1 shows that the purple color intensity decreases with increasing aluminum content. Since the samples have similar thicknesses around 1 mm, this behavior could be a consequence of the decrease in the concentration of titanium in the material (Table 1).

The glass transition temperature of NATP precursor glasses, T_g, is indicated as a change in the baseline in the endothermic direction (see Fig. 2-a). The exothermic peak is ascribed to the glass crystallization, and the onset temperature, T_x, indicates the beginning of the crystallization process (Fig. 2-b). The presence of a narrow and sharp single peak, except in $x = 1.4$ (NATP14) composition, is indicative of the formation of a single crystalline phase, as expected. It can also be observed that the crystallization peak is very sharp (except in $x = 1.4$), indicating that precursor glasses have a great tendency to crystallize due to rapid crystallization kinetics. Table 2 summarizes the T_g and T_x values obtained from DSC curves in Fig. 2.

It can be seen that both the glass transition temperature and the crystallization temperature shift to lower temperatures as the concentration of aluminum increases (see Table 2). Ortiz-Mosquera et al. [11] observed the same tendency of T_g for the homologous glasses containing germanium instead of titanium ($Na_{1+x}Al_xGe_{2-x}(PO_4)_3$). We recall here that the substitution of titanium by aluminum ion in the $Na_{1+x}Al_xTi_{2-x}(PO_4)_3$ formula generates an excess of negative charge, which must be compensated by the inclusion of Na^+ ions from sodium oxide (Na_2O). Thus, as x increases, both aluminum and sodium ion content increases. The inclusion of sodium oxide leads to the break of P—O—P bonds to allow the introduction of the extra oxygen from the alkali metal oxide, and consequently, the number of non-bridging oxygen increases, thus decreasing T_g.

On the other hand, the parameter T_x - T_g, which indicates the thermal stability of the glass against crystallization and also the glass-forming ability [17], increases when x increases. Therefore, we can infer that the incorporation of aluminum favors the tendency for glass formation. Furthermore, it has been demonstrated that low percentages of TiO_2 favor the glass formability in phosphate glasses, because the titanium ion forms Ti—O—P bonds between the phosphate tetrahedra, thus strengthening the glass network [18]. In fact, it was observed experimentally that the tendency for the crystallization of the precursor liquid during the synthesis of the NATP glasses decreased for compositions with higher aluminum content.

Table 2
Characteristic temperatures of NATP precursor glasses: glass transition temperature (T_g), crystallization temperature (T_x), and stability parameter (T_x - T_g).

Sample	T_g (K) (±2 K)	T_x (K) (±2 K)	T_x - T_g (K)
NATP00	–	–	–
NATP04	950	992	42
NATP06	918	970	52
NATP08	876	949	73
NATP10	845	940	95
NATP12	813	910	97
NATP14	786	916	130

3.2. X-ray diffraction (XRD)

The absence of diffraction peaks in the X-ray pattern of $x = 0.6$ parent glass confirms its amorphous nature (Fig. 3-a). Similar behavior was also evidenced for all other aluminum-containing vitreous samples. The amorphous halo between $20° < 2\theta < 30°$ is typical for phosphate NASICON glasses [8,9,11].

Fig. 3-a also shows the XRD structural evolution of $Na_{1+x}Al_xTi_{2-x}(PO_4)_3$ glass-ceramic samples as a function of the amount of aluminum. The $NaTi_2(PO_4)_3$ NASICON phase (ICSD 290798), is observed as the unique phase present in the glass-ceramics in the composition range of $0.0 \leq x \leq 1.0$. This fact suggests that all Al^{+3} ions were included in the NASICON structure, replacing Ti^{+4} and forming a solid solution. However, small peaks of $AlPO_4$ as a secondary phase (ICSD 280308, open ball) are observed in samples with $x = 1.2$ (NATP12) and 1.4 (NATP14) composition. The Rietveld refinement of the X-ray pattern of these samples reveals that the amount of the secondary phase does not exceed 5 wt % in both cases (see Table 3). The presence of the $AlPO_4$ phase in NASICON compounds, when titanium ions are replaced by aluminum ions, was also reported in previous works [9,10,19]. In addition, the spurious phase observed in samples for $x \geq 1.2$ indicates that the limit of the solid solution of aluminum is reached for $x = 1.0$ (NATP10). On the other hand, the shoulder in the near-right of the most intense peak ($2\theta = 24°$) in the NATP10 sample also corresponds to the NASICON phase as analyzed by Rietveld refinement. In fact, this shoulder becomes a peak with the inclusion of more

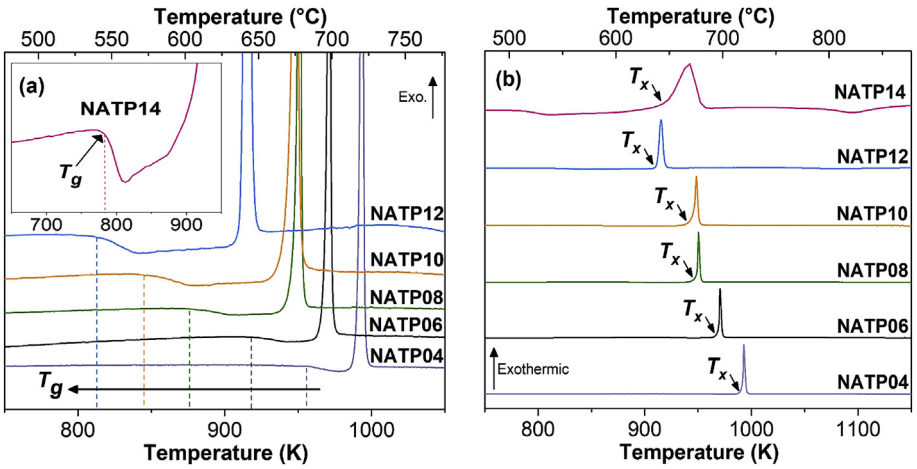

Fig. 2. DSC thermograms of NATP precursor glasses, indicating (a) the glass transition temperature (T_g) and (b) the onset of the crystallization peak (T_x).

Please cite this article as: A.M. Nieto-Muñoz et al., The role of Al^{+3} on the microstructural and electrical properties of $Na_{1+x}Al_xTi_{2-x}(PO_4)_3$ NASICON glass-ceramics, Journal of Alloys and Compounds, https://doi.org/10.1016/j.jallcom.2019.153148

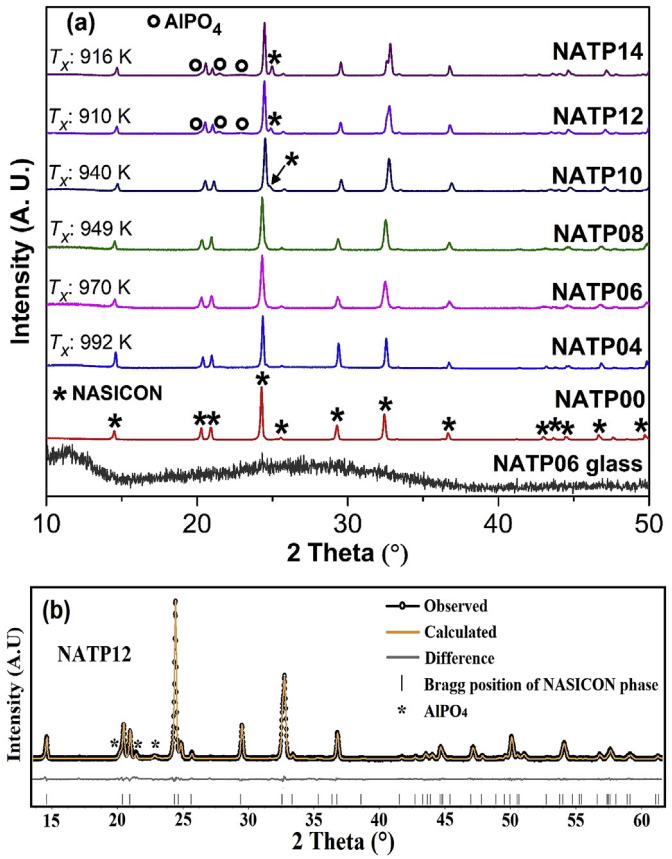

Fig. 3. (a) X-ray diffractograms of NATP glass-ceramics obtained by heat treatment of precursor glasses at their respective T_x (see Table 2) for 30 min. (b) Rietveld refinement of X-ray pattern of the NATP12 glass-ceramic. The agreement factors are: $R_{wp} = 10.16\%$, $R_p = 6.88\%$.

Table 3
Unit cell parameters, secondary phase content ($AlPO_4$), R factors (R_{wp} and R_p) of $x = 1.2$ (NATP12) and $x = 1.4$ (NATP14) glass-ceramics.

Sample	a	c	V	$AlPO_4$	R_{wp}	R_p
	Å	Å	Å^3	wt. %	%	%
NATP10[a]	8.46	21.60	1339	0.0	-	-
NATP12	8.4789 (7)	21.530 (2)	1338.5 (2)	4.2 (1)	10.16	6.88
NATP14	8.4813 (3)	21.457 (1)	1336.7 (1)	4.4 (1)	9.53	6.76

[a] Data from Ref. [20].

aluminum in the NATP12 and NATP14 samples.

In our previous work [20], we showed from the Rietveld Analysis of samples with $x \leq 1.0$ that the partial replacement of titanium by aluminum ions causes the contraction of the NASICON unit cell. Extending the Rietveld analysis to samples with $x > 1.0$, it can be observed that this trend is maintained although the solid solution limit has already been reached (see Table 3). As an example, Fig. 3-b shows the result of the Rietveld refinement for $x = 1.2$ sample. The decrease in the unit cell volume in the $Na_{1+x}Al_xTi_{2-x}(PO_4)_3$ series is attributed to the difference between the ionic radii from Ti^{+4} (0.605 Å) and Al^{+3} ion (0.535 Å). Mouahid et al. [10] also observed a contraction of the cell volume in the same NASICON system obtained by solid-state reaction. These authors concluded that the inclusion of aluminum in the MO_6 octahedron of the NASICON structure decreases the M − O distance along the c-axis, which is reflected in the shortening of the "c" parameter, while the "a" parameter remains constant.

3.3. Scanning electronic microscopy (SEM)

SEM micrographs of fractured surfaces of $Na_{1+x}Al_xTi_{2-x}(PO_4)_3$ ($0.6 \leq x \leq 1.4$) glass-ceramics confirm the crystallization of parent glasses (see Fig. 4). All samples exhibit low porosity and uniform microstructure. In addition, it can be observed that the average grain size increases with the addition of aluminum. Samples with $x = 0.6$ (Fig. 4-a) and $x = 0.8$ (Fig. 4-b) show the formation of rounded grains with an average size of approximately 300 nm and 500 nm, respectively. Medium-sized grains on the order of microns lose the rounded shape in NATP10 and NATP12 samples (Fig. 4 c-d). Furthermore, the NATP12 sample displays the presence of asymmetric grains with a size between 18 and 20 μm. A zoom in the micrograph of this sample shows that grains are composed of micrometric substructures with a parallelepipedal-shape and right angles. As can be seen in Fig. 4-e, the largest average grain size of the NATP series was reached in the NATP14 glass-ceramic. Cubic grains were obtained in this composition with a size around 20–30 μm.

3.4. Complex impedance spectroscopy

The complex plane plot of impedance data ($-Z''$ vs. Z'), also called the Nyquist plot (Fig. 5), of all glass-ceramics under investigation, shows a depressed semicircle at high and medium frequencies. This characteristic indicates a strong overlap of the grain and grain boundary contributions. The grain contribution is seen as a distortion at higher frequencies of the depleted semicircle, except for the NATP00 sample, for which the semicircles of both contributions (grain and grain boundary) are well separated. An inclined spike is also observed at low frequencies, which is ascribed to the ion blockage at the electrolyte-electrode interface, thus confirming that the conductivity of the samples is of ionic nature. Nevertheless, for the free-aluminum NATP00 composition (Fig. 5-b), the spike at low frequencies is parallel to the Z'-axis, thus suggesting that the electrode is not blocking. In fact, low values of electronic conductivity have already been observed in the compound $NaTi_2(PO_4)_3$ by other authors [21,22], which may be the cause of this behavior at low frequencies.

Note that all Z'' and Z' data in Fig. 5 were corrected by the geometric factor of each sample to allow a comparison between them. Thus, the total resistivity (ρ) of the sample can be directly known by the intercept at low frequencies of the semicircle to the x-axis. Accordingly, the total ionic conductivity (σ) can be calculated through the ratio: $\sigma = 1/\rho$.

Conventional Arrhenius plots of conductivity data were obtained in the temperature range of 50 °C − 300 °C for all glass and glass-ceramic samples, as shown in Fig. 6. In this temperature range, a linear behavior of electrical conductivity is observed. It should be noted that the linear regression of all Arrhenius plots presented a correlation factor (> 0.999), indicating a high degree of precision in the collected data. The activation energy (E_a), the logarithm of the pre-exponential factor ($\log \sigma_0$) and total conductivity at 300 °C ($\sigma_{300\ °C}$) were determined from the linear regression of the data in Fig. 6 using the logarithm form of the Arrhenius equation:

$$\log \sigma = \log \sigma_0 - \log e^{*}(E_a / kT) \quad (1)$$

where E_a is the activation energy, σ_0 is the pre-exponential term, k and T have their usual meaning, and e is the Euler's number. The pre-exponential constant, σ_0, is related to the ionic charge (Ze, where Z is the ion valence and e, the electron charge), the total concentration of the ions (n), the hopping frequency (ν_0) and the hopping distance (λ) according to Equation (2) [23,24]:

Please cite this article as: A.M. Nieto-Muñoz et al., The role of Al^{+3} on the microstructural and electrical properties of $Na_{1+x}Al_xTi_{2-x}(PO_4)_3$ NASICON glass-ceramics, Journal of Alloys and Compounds, https://doi.org/10.1016/j.jallcom.2019.153148

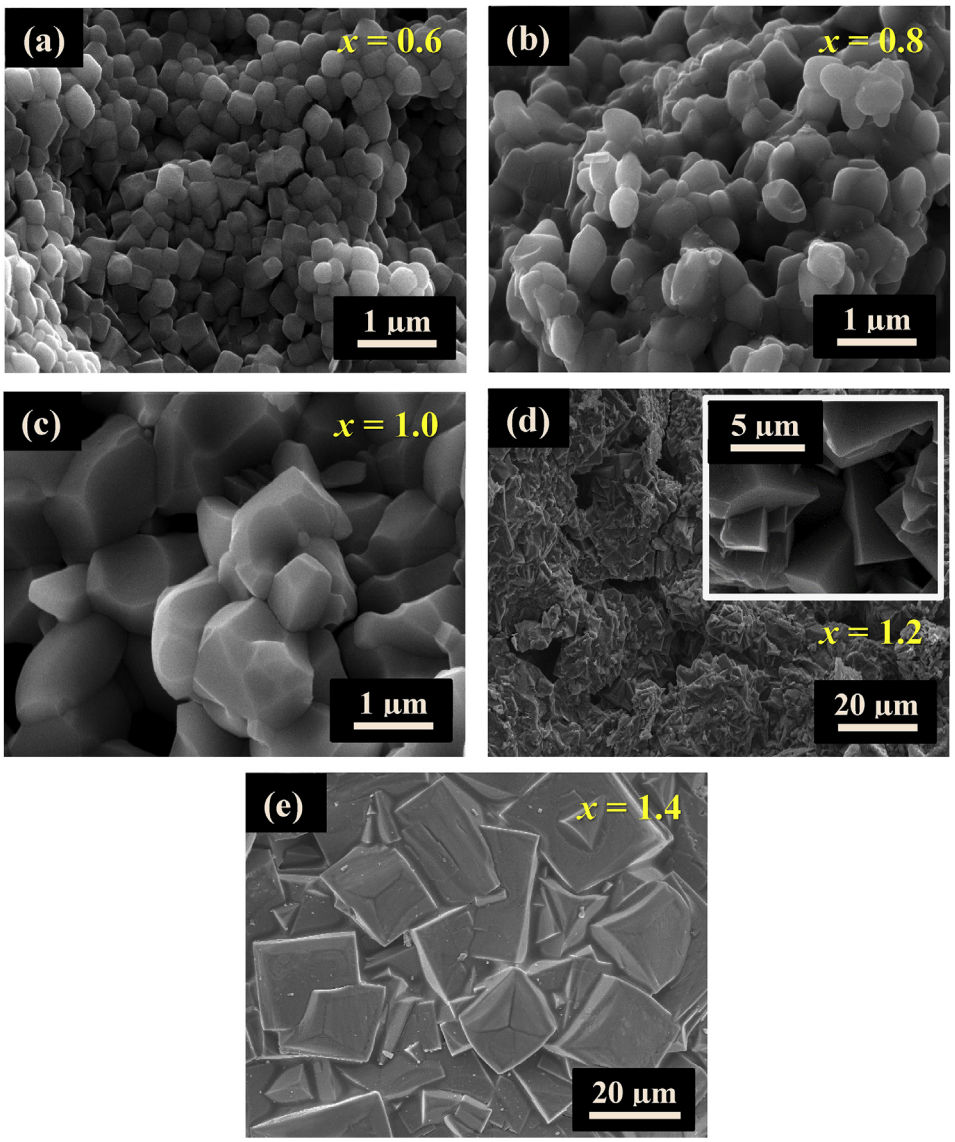

Fig. 4. SEM results of fracture surface of NATP glass-ceramic samples (a) NATP06, (b) NATP08, (c) NATP10, (d) NATP12 and (e) NATP14 obtained by heat treatment at respective T_x (see Table 2) for 30 min.

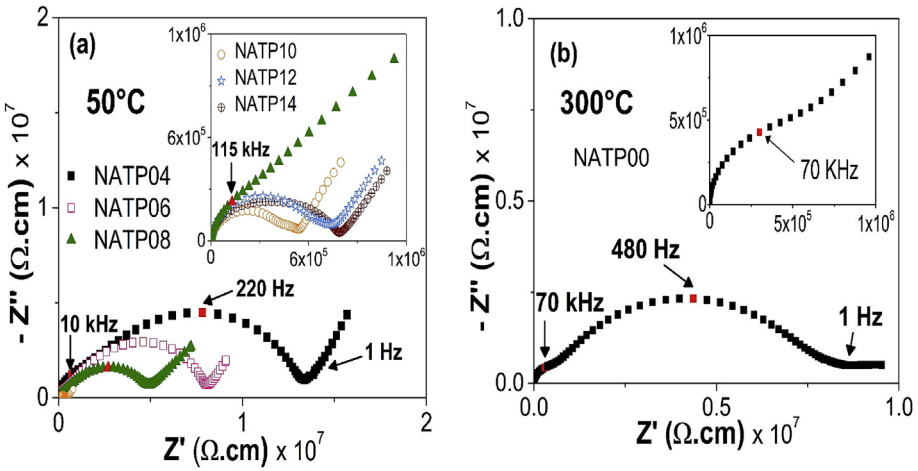

Fig. 5. Complex impedance plot of $Na_{1+x}Al_xTi_{2-x}(PO_4)_3$ (NATP) glass-ceramics for (a) $0.4 \leq x \leq 1.4$ at 50 °C and (b) $x = 0.0$ (NATP00) at 300 °C.

Please cite this article as: A.M. Nieto-Muñoz et al., The role of Al^{+3} on the microstructural and electrical properties of $Na_{1+x}Al_xTi_{2-x}(PO_4)_3$ NASICON glass-ceramics, Journal of Alloys and Compounds, https://doi.org/10.1016/j.jallcom.2019.153148

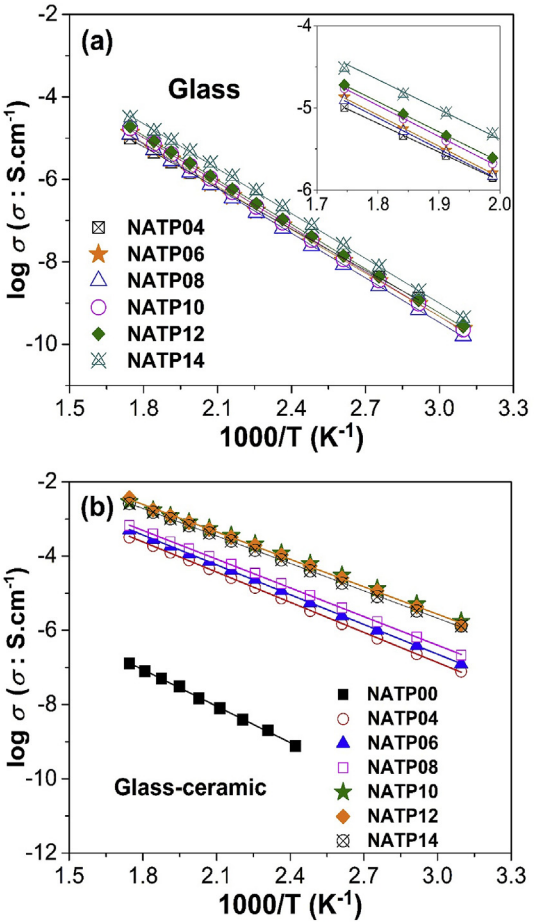

Fig. 6. Arrhenius plot of total ionic conductivity of NATP (a) glasses and (b) glass-ceramics as a function of the inverse of the temperature, 1000/*T*. The lines represent the linear regression of experimental data. Error bars are smaller than the data symbols.

$$\sigma_0 \approx n(Ze)^2\lambda^2\nu_0 \,/\, kT \qquad (2)$$

All values related to the Arrhenius equation are presented in Table 4.

Although the nominal molar concentration of modifier Na_2O varies from 17.5 to 30.0, for x varying from 0.4 to 1.4 in this series (see Table 1), the activation energy (E_a) and the total ionic conductivity at 300 °C ($\sigma_{300°C}$) of NATP parent glasses do not present significant variations with the increase of x. This is indicative of a concurrent effect of Na_2O and Al_2O_3 oxides in the ionic conductivity of these glasses. While the sodium oxide increases both the concentration of Na^+ charge carrier and non-bridging oxygen, aluminum oxide plays an inverse role creating Al—O—P linkages [25]. The calculated pre-exponential factors for the precursor glasses vary from 0.8 to 1.9 and they are consistent with the experimental data found in precursor glasses from other NASICON systems [9,11] and other ionic conducting glasses [26,27].

In relation to the electrical behavior of the glass-ceramics, it is evident that the ionic conductivity increases by up to two orders of magnitude in relation to their respective precursor glasses (see Table 4 and Fig. 6-b). As expected, the formation of the NASICON phase after heat treatment facilitates the movement of Na^+ ions, due to its structure with 3D channels, thus causing a decrease in the activation energy required for ion migration. It can be observed in Fig. 7 that the activation energy values of $Na_{1+x}Al_xTi_{2-x}(PO_4)_3$ glass-ceramics decrease significantly when aluminum and sodium ions (x) are introduced. Because the pre-exponential factor (σ_0) does not vary significantly, the decrease in the activation energy leads to an increase in the ionic conductivity by up to four orders of magnitude when compared to the NATP00 free-aluminum sample. However, it is also noted that the conductivity does not improve for compositions with $x > 1.0$ (NATP10). It is possible that the conduction channel size is not suitable for the displacement of Na^+ ions for compositions with $x > 1.0$, i.e., a very narrow channel, which would be a consequence of the contraction of the NASICON unit cell observed and discussed in Section 3.2. This behavior is also reflected in the increase of activation energy in $x = 1.2$ and 1.4

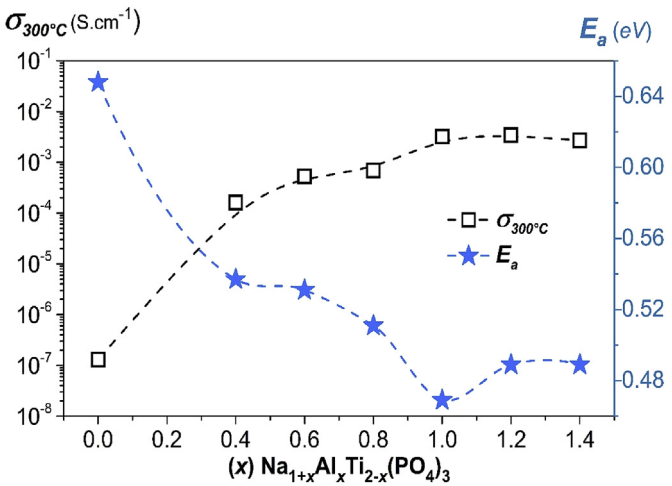

Fig. 7. Total ionic conductivity at 300 °C ($\sigma_{300°C}$) and activation energy (E_a) as a function of aluminum content (x) in $Na_{1+x}Al_xTi_{2-x}(PO_4)_3$ glass-ceramics. Dashed lines serve as a guide for the eyes. Error bars are smaller than the data symbols.

Table 4
Total ionic conductivity at 300 °C ($\sigma_{300°C}$), activation energy (E_a) and the logarithm of pre-exponential factor (log σ_0), of NATP glass and glass-ceramic samples. The numbers between parentheses indicate the mathematical errors given by the linear regression of data.

Sample	Glasses			Glass-ceramics		
	E_a (*eV*)	$\sigma_{300°C}$ (S.cm^{-1})	log σ_0 (σ_0: S.cm^{-1})	E_a (*eV*)	$\sigma_{300°C}$ (S.cm^{-1})	log σ_0 (σ_0: S.cm^{-1})
NATP00	–	–	–	0.648 (7)	1.3×10^{-7}	−1.17 (8)
NATP04	0.659 (4)	9.5×10^{-6}	0.77 (4)	0.537 (2)	1.6×10^{-4}	0.91 (2)
NATP06	0.694 (4)	1.2×10^{-5}	1.18 (4)	0.531 (2)	5.3×10^{-4}	1.39 (6)
NATP08	0.715 (2)	1.2×10^{-5}	1.35 (2)	0.511 (2)	6.9×10^{-4}	1.34 (4)
NATP10	0.715 (3)	1.6×10^{-5}	1.50 (3)	0.469 (5)	3.2×10^{-3}	1.64 (4)
NATP12	0.710 (2)	1.8×10^{-5}	1.51 (2)	0.489 (4)	3.4×10^{-3}	1.83 (5)
NATP14	0.718 (4)	3.6×10^{-5}	1.87 (4)	0.489 (2)	2.7×10^{-3}	1.72 (2)

Please cite this article as: A.M. Nieto-Muñoz et al., The role of Al^{+3} on the microstructural and electrical properties of $Na_{1+x}Al_xTi_{2-x}(PO_4)_3$ NASICON glass-ceramics, Journal of Alloys and Compounds, https://doi.org/10.1016/j.jallcom.2019.153148

samples. In our previous works about Li^+ [9] and Na^+ [11] -ion-conducting NASICON glass-ceramics, it is shown that the $AlPO_4$ phase in low quantities does not affect the ionic conductivity of the material. Thus, it may be argued that, the presence of the $AlPO_4$ phase (around 4 wt % in NATP12 and NATP14) does not significantly impair the electrical properties of these two samples.

The E_a and total ionic conductivity values shown in Table 4 for glass-ceramics are in good agreement with the results obtained by Mouahid et al. [10] for the same composition synthesized by solid state reaction, thus indicating that, in the present case, the glass-ceramic route did not promote significant changes in the total ionic conductivity of the material.

It is worth mentioning that the addition of aluminum has also been analyzed in the analogous $Na_{1+x}Al_xGe_{2-x}(PO_4)_3$ (NAGP) glass-ceramic system [11]. The highest ionic conductivity (2.3×10^{-4} S cm^{-1} at 300 °C) for this NASICON series was achieved at composition $x = 0.8$, and is one order of magnitude lower than the conductivity exhibited by the most conductive sample in the present work (see Table 4). The difference between the ionic conductivity values of both systems is probably due to the smaller volume of the NAGP series unit cell which is reflected in higher activation energy values when compared to that of the titanium-containing series, i.e., the bottleneck through which the sodium ion moves has a more suitable size in the NATP than in the NAGP system.

On the other hand, the increase in average grain size observed in the glass-ceramic samples (see Section 3.3) may also be responsible for the increase in the overall ionic conductivity, since it would reduce the number of grain boundaries (N_{gb}) according to the expression: $N_{gb} = L/d_g$ (d_g is the average grain size and L, the sample thickness) [28].

3.5. Grain and grain boundary contributions

The Nyquist plots in Fig. 5 (Section 3.4) show that the grain boundary response dominates the total impedance of the sample since the semicircle associated with the grain (in high frequency) is not clearly visible, i.e., it has a lower diameter than the semicircle attributed to the grain boundary. Thus, the modulus formalism (M^*) was used to facilitate the visualization and analysis of each one of the contributions (grain and grain boundary) in the material. The electrical modulus, M^*, is related to the impedance, $Z^* = Z' - iZ''$, according to Equation (3):

$$M^* = i\omega C_0 Z^* \tag{3}$$

where $C_0 = \varepsilon_0 A/L$ is the empty cell capacitance, ω is the angular frequency ($2\pi f$), ε_0 is the dielectric permittivity of the vacuum, A is the area of the sample and L is the separation between the electrodes, or in the present case, the sample thickness. Thus, the real (M') and imaginary (M'') part of the electric modulus are represented by the expressions: $M' = \omega C_0 Z''$ and $M'' = i\omega C_0 Z'$, respectively.

From the spectroscopic diagrams, i.e., the imaginary part of impedance (Z'') and modulus (M'') as a function of frequency (f), two different Debye peaks can be observed. Each of them emphasizes different contributions within the material. The Z'' vs. log f plot is dominated by the most resistive contributions within the material [29,30] since Z'' depends proportionally on the resistance (R) according to Equation (4), which in our case would be the component associated with the grain boundary.

$$Z'' = R\,[\omega RC / (1 + (\omega RC)^2)] \tag{4}$$

On the other hand, the formalism of the electric modulus emphasizes the contribution of lower capacitance (C) [29,30], which in our case would correspond to the contribution of the grain, as follows:

$$M'' = \varepsilon_0 / C\,[\omega RC / (1 + (\omega RC)^2)] \tag{5}$$

Thus, contributions related to the electrode-sample interface and grain boundary are generally not seen in the M'' modulus plot because these both contributions are associated with higher capacitances.

An important feature of the spectroscopic plots is that the Z''_{max} is equal to $R/2$ and, the maximum M''_{max} corresponds to $1/2C$. Thus, the grain boundary resistivity and the grain capacitance can be calculated from Z''_{max} and M''_{max}, respectively. Because each Debye peak is in turn associated with a relaxation frequency ($\omega = \omega_p$) according to the expression: $\omega_p = 1/RC$, it is also possible to know the grain-boundary capacitance and the grain resistivity.

Fig. 8a–b shows the Z'' and M'' diagrams for glass-ceramics with $x = 0.0$ (NATP00) and $x = 0.8$ (NATP08) at 300 °C and 50 °C, respectively. In both cases, a maximum is observed in each curve as expected. The Z''_{max} maximum in the Z'' plot (left axis) is located at the lower frequency region and the M''_{max} is located at the higher frequencies (> 10 kHz, right axis). It can be noted that the difference in relaxation frequencies between both peaks is around two decades in both cases, thus indicating that each peak results from two different electrical responses [31,32].

The capacitances at the peak frequency from Z''_{max} and M''_{max} were also calculated and are indicated in Fig. 8a–b. A difference around one order of magnitude is observed between the capacitance values associated with each peak for both samples, NATP00 (without aluminum) and NATP08. Similar results (not shown here) were obtained for the compositions $x = 0.4$ and 0.6. The capacitance values estimated from Z''_{max} (~ 6×10^{-11} F at low frequencies) and M''_{max} (3 to 5×10^{-12} F at high frequencies) are in accordance with the capacitance range proposed by Irvine et al. [22], for grain boundary and grain phenomena, respectively. Thus, it can be confirmed that the distortion effect seen at high frequencies in the Nyquist diagram for the samples containing aluminum (Fig. 5-a) is related to the electrical contribution of the grain. Note that, as expected, this distortion effect is not seen at high frequencies in the Z'' spectroscopic plot of the NATP08 sample (Fig. 8-b). However, in the spectroscopic chart of the free-aluminum sample, a shoulder can be observed around 10^5 Hz in the Z'' plot. This is justified because the semicircle at high frequencies attributed to the grain is better formed in the Nyquist plot of this same sample (Fig. 5-b) compared to the aluminum-containing sample diagrams.

In relation to the NATP10, NATP12 and NATP14 samples, a difference lower than 0.5 orders of magnitude in the frequency associated with the Z'' and M'' peaks (not shown here), was observed thus indicating that both peaks result from the same contribution (intrinsic material response), i.e., no individual grain and grain boundary responses could be detected for those samples, thus these results were excluded from the following discussion.

To further confirm the separation of grain and grain boundary in $Na_{1+x}Al_xTi_{2-x}(PO_4)_3$ glass-ceramics with $x = 0.0$ to 0.8, impedance data were also converted to the C^* formalism ($C^* = C' - iC''$). This formalism analyzes the losses in the form of energy dissipation and the capacitive behavior of the samples with the application of an alternating current [33]. The complex capacitance, C^*, is related to the frequency and impedance, Z^*, according to the expression:

$$C^* = 1/j\omega Z^* \tag{6}$$

By substitution of $Z^* = Z' - iZ''$, the real (C') and imaginary part (C'') of capacitance is:

Please cite this article as: A.M. Nieto-Muñoz et al., The role of Al^{+3} on the microstructural and electrical properties of $Na_{1+x}Al_xTi_{2-x}(PO_4)_3$ NASICON glass-ceramics, Journal of Alloys and Compounds, https://doi.org/10.1016/j.jallcom.2019.153148

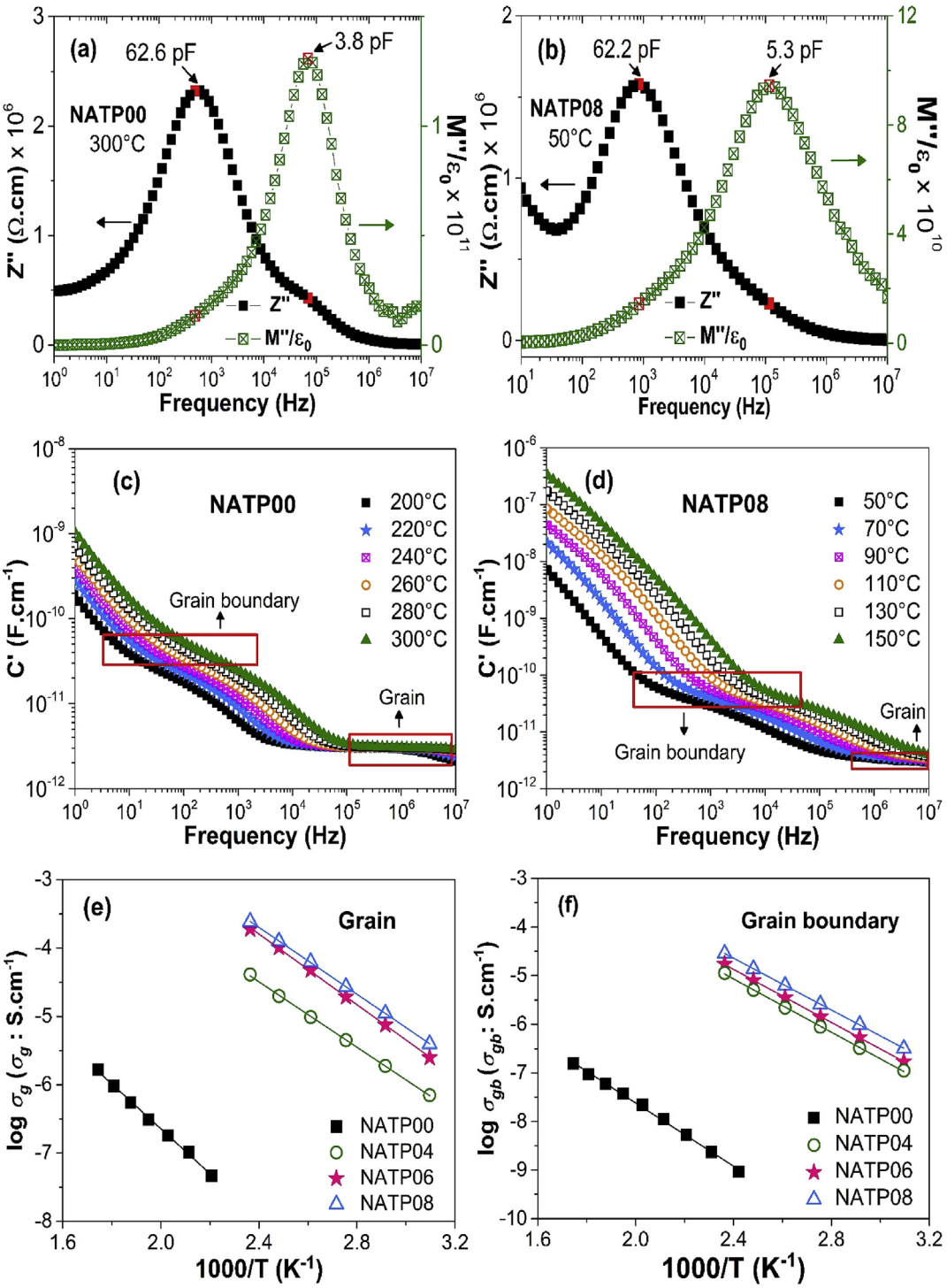

Fig. 8. Impedance (Z'') and electric modulus (M'') plots as a function of log f for (a) NATP00 and (b) NATP08 glass-ceramics. Real part of complex capacitance (C') vs. log f for (c) NATP00 and (d) NATP08 samples. Arrhenius plots of (e) grain and (f) grain boundary of NATP glass-ceramic samples. The lines in (e) and (f) represent the linear regression of experimental data. Error bars are smaller than the data symbols.

$$C' = Z'' / \omega(Z'^2 + Z''^2) \quad (7)$$

$$C'' = - Z' / \omega(Z'^2 + Z''^2) \quad (8)$$

The real part of the complex capacitance (C'), as a function of the frequency on a double-logarithmic scale at different temperatures, is plotted for $x = 0.0$ and 0.8 samples in Fig. 8c–d. These graphs show two relaxation processes (plateau) for both compositions at all temperatures. The first relaxation process occurring at medium frequencies, between 10 to 10^3 *Hz* corresponds to a capacitance around 60 *pF*, which coincides with the capacitance indicated at the maximum of Z'' vs. f plot (Fig. 8a–b), thus confirming the attribution of this peak to the grain boundary. A second plateau is seen at higher frequencies ($10^5 - 10^7$ *Hz*) with a capacitance around 3 –

Please cite this article as: A.M. Nieto-Muñoz et al., The role of Al^{+3} on the microstructural and electrical properties of $Na_{1+x}Al_xTi_{2-x}(PO_4)_3$ NASICON glass-ceramics, Journal of Alloys and Compounds, https://doi.org/10.1016/j.jallcom.2019.153148

Table 5
Activation energy of grain ($E_{a\text{-}g}$) and grain boundary ($E_{a\text{-}g}$), grain ($\sigma_{g\text{-}100^{\circ}C}$) and macroscopic grain boundary conductivity at 100 °C ($\sigma_{gb\text{-}100^{\circ}C}$), logarithm of pre-exponential factor of grain (log $\sigma_{0\text{-}g}$) and grain boundary (log $\sigma_{0\text{-}b}$) of NATP glass-ceramics. Indicated uncertainties are the mathematical errors calculated from the linear regression.

Sample	Grain			Grain boundary		
	$E_{a\text{-}g}$ (eV)	$\sigma_{g\text{-}100^{\circ}C}$ ($S.cm^{-1}$)	log $\sigma_{0\text{-}g}$ ($\sigma_{0\text{-}g}$: $S.cm^{-1}$)	$E_{a\text{-}gb}$ (eV)	$\sigma_{gb\text{-}100^{\circ}C}$ ($S.cm^{-1}$)	log $\sigma_{0\text{-}gb}$ ($\sigma_{0\text{-}gb}$: $S.cm^{-1}$)
NATP00	0.650 (9)	1.3×10^{-9}	−0.09 (9)	0.645 (9)	1.5×10^{-10}	−1.11 (9)
NATP04	0.475 (5)	6.9×10^{-6}	1.25 (6)	0.543 (6)	1.5×10^{-6}	1.50 (8)
NATP06	0.512 (5)	3.1×10^{-5}	2.41 (7)	0.540 (3)	2.3×10^{-6}	1.67 (4)
NATP08	0.484 (2)	4.2×10^{-5}	2.17 (3)	0.527 (2)	4.1×10^{-6}	1.75 (2)

5 *pF*, and it is attributed to the grain contribution since this *C* value is similar to that calculated from the M'' peak in the spectroscopic plots of Fig. 8a–b. Between those two plateaus, the increase in the C' value from higher to lower frequencies (10^4 to 10^2 *Hz*) indicates a blocking of Na^+ ions, in the intergranular or grain boundary region. Finally, at very low frequencies ($< 10^2$ *Hz*), the increase in the C' capacitance as frequency decreases is ascribed to the Na^+ ions being blocked at the electrolyte-electrode interface.

After confirming the attribution of the grain and grain boundary contributions in Fig. 8a–d, the grain (σ_g) and macroscopic grain boundary (σ_{gb}) ionic conductivities were calculated from the resistivity data associated respectively to M''_{max} and Z''_{max}, for $x = 0.0$ to 0.8 samples. Fig. 8e–f shows the Arrhenius plots and Table 5 summarizes the data of activation energy, ionic conductivity and pre-exponential factor for both contributions.

It is worth noting from Fig. 8e–f and Table 5 that the first addition of aluminum ($x = 0.4$) leads to a significant increase in the ionic conductivity of both the grain and grain boundary. In fact, including aluminum in the NATP system promotes the decrease of grain ($E_{a\text{-}g}$) and grain boundary ($E_{a\text{-}gb}$) activation energy as compared to the aluminum-free sample (NATP00) thus, favoring the ionic conductivity in both regions. It can also be noted that the grain boundary dominates the electrical response of the material since its activation energy is higher than that of the grain and particularly, because this value is similar to the activation energy for the total ionic conductivity (see Table 4). For the NATP00 sample, no significant differences are observed between these two activation energies ($E_{a\text{-}g}$ and $E_{a\text{-}gb}$), inferring that the conduction mechanisms are similar in the grain and grain boundary in this sample.

Table 5 also shows that the increase in the grain conductivity is mostly influenced by an increase in the pre-exponential factor since the activation energy does not change markedly in the aluminum-containing samples. As mentioned previously, since the pre-exponential factor depends on the number of charge carriers, an increase in this value is expected with the gradual inclusion of Na^+ ions because of the increase of x (see Equation (2)).

In the case of the intergranular region, beyond the increase in the pre-exponential factor, a small decrease in the activation energy is also observed when x increases. Both parameters contribute to the higher ionic conductivity in the compositions with a larger amount of aluminum (σ_{gb}, see Table 5). In both cases (grain and grain boundary), an increase can be observed of up to four orders of magnitude in ionic conductivity with the inclusion of aluminum.

4. Conclusions

In this study, we have demonstrated the glass-ceramic route as a synthesis method for the $Na_{1+x}Al_xTi_{2-x}(PO_4)_3$ NASICON series ($0.0 < x \leq 1.4$). The experimental data show that adding aluminum to the $NaTi_2(PO_4)_3$ system favors the formability of the precursor glasses. The crystallization of samples results in the formation of the NASICON phase in the whole investigated composition range. It was also observed that NASICON is the only phase crystallized in compositions with $x \leq 1.0$, thereby demonstrating that the Al-solubility limit is reached when $x = 1.0$. By complex impedance spectroscopy, it was shown that the inclusion of aluminum in the NASICON structure increased the ionic conductivity by up to five orders of magnitude when compared to the free-aluminum sample. The highest ionic conductivity was reached in the glass-ceramic with composition $x = 1.0$. The contributions of grain and grain boundary in the ionic conductivity were separated using the formalism of the electric modulus for $x = 0.0$ to 0.8. It was noted that the grain boundary dominates the electrical response of the material because it exhibits higher activation energy than the grain. However, an increase in the average grain size of the samples with a higher concentration of aluminum was also observed, which also favors the total ionic conductivity. Finally, it was observed that the increase in charge carriers concentration (Na^+) generated by the inclusion of aluminum ions promoted the increase in conductivity in both the grain and grain boundary regions.

Author contribution section

AMNM designed the study; AMNM and JFOM carried out the experiments and characterizations; AMNM and JFOM contributed to sample preparation; AMNM wrote the manuscript and designed the figures; AMNM performed the Rietveld analysis; JFOM and ACMR contributed to the interpretation of the results and worked on the manuscript; ACMR supervised the project; All authors provided critical feedback and helped shape the research, analysis and manuscript.

Declaration of competing interest

The authors declare that they have no known competing financial interests or personal relationships that could have appeared to influence the work reported in this paper.

Acknowledgments

The authors gratefully acknowledge the financial support of the Brazilian research funding agencies FAPESP (Fundação de Amparo à Pesquisa do Estado de São Paulo, Process No. 2013-07793, via the CEPID program), CNPq (Conselho Nacional de Desenvolvimento Científico e Tecnológico, under Process No. 141220/2016-3 for AMNM and Process No. 168682/2017–6 for JFOM), and CAPES (Coordenação de Aperfeiçoamento de Pessoal de Nível Superior), Brazil, Finance code 001.

References

[1] F. Lalère, J.B. Leriche, M. Courty, S. Boulineau, V. Viallet, C. Masquelier, V. Seznec, An all-solid state NASICON sodium battery operating at 200°C, J. Power Sources 247 (2014) 975–980, https://doi.org/10.1016/

j.jpowsour.2013.09.051.
[2] Y. Noguchi, E. Kobayashi, L.S. Plashnitsa, S. Okada, J.I. Yamaki, Fabrication and performances of all solid-state symmetric sodium battery based on NASICON-related compounds, Electrochim. Acta 101 (2013) 59–65, https://doi.org/10.1016/j.electacta.2012.11.038.
[3] D. Kundu, E. Talaie, V. Duffort, L.F. Nazar, The emerging chemistry of sodium ion batteries for electrochemical energy storage, Angewandte, Angew. Chemie Int. Ed. 54 (2015) 3431–3448, https://doi.org/10.1002/anie.201410376.
[4] J.F. Ortiz-Mosquera, A.M. Nieto-Muñoz, H. Bradtmüller, H. Eckert, A.C.M. Rodrigues, Isothermal evolution of phase composition, structural parameters, and ionic conductivity in Na1+xAlxGe2-x(PO4)3 glass-ceramics (In Press), J. Non-Cryst. Solids 528 (2020), https://doi.org/10.1016/j.jnoncrysol.2019.119725.
[5] J.B. Goodenough, H.-P. Hong, J.A. Kafalas, Fast Na+-ion transport in skeleton structures, Mater. Res. Bull. 11 (1976) 203–220, https://doi.org/10.1016/0025-5408(76)90077-5.
[6] M. Guin, F. Tietz, Survey of the transport properties of sodium superionic conductor materials for use in sodium batteries, J. Power Sources 273 (2015) 1056–1064, https://doi.org/10.1016/j.jpowsour.2014.09.137.
[7] J. Fu, Superionic conductivity of glass-ceramics in the system Li2O-Al2O3-TiO2-P2O5, Solid State Ion. 96 (1997) 195–200, https://doi.org/10.1016/S0167-2738(97)00018-0.
[8] A.M. Nieto-Muñoz, J.F. Ortiz-Mosquera, A.C.M. Rodrigues, Novel sodium superionic conductor of the Na1+yTi2SiyP3-yO12 series for application as solid electrolyte, Electrochim. Acta 319 (2019) 922–932, https://doi.org/10.1016/j.electacta.2019.07.032.
[9] J.L. Narváez-Semanate, A.C.M. Rodrigues, Microstructure and ionic conductivity of Li1+xAlxTi2-x(PO4)3 NASICON glass-ceramics, Solid State Ion. 181 (2010) 1197–1204, https://doi.org/10.1016/j.ssi.2010.05.010.
[10] F.E. Mouahid, M. Bettach, M. Zahir, P. Maldonado-Manso, S. Bruque, E.R. Losilla, M.A.G. Aranda, Crystal chemistry and ion conductivity of the Na1+xTi2−xAlx(PO4)3 ($0 \leq x \leq 0.9$) NASICON series, J. Mater. Chem. 10 (2000) 2748–2757, https://doi.org/10.1039/b004837m.
[11] J.F. Ortiz-Mosquera, A.M. Nieto-Muñoz, A.C.M. Rodrigues, Precursor glass stability, microstructure and ionic conductivity of glass-ceramics from the Na1+xAlxGe2−x(PO4)3 NASICON series, J. Non-Cryst. Solids 513 (2019) 36–43, https://doi.org/10.1016/j.jnoncrysol.2019.03.008.
[12] A.M. Cruz, E.B. Ferreira, A.C.M. Rodrigues, Controlled crystallization and ionic conductivity of a nanostructured LiAlGePO4 glass-ceramic, J. Non-Cryst. Solids 355 (2009) 2295–2301, https://doi.org/10.1016/j.jnoncrysol.2009.07.012.
[13] Oxford Cryosystems, J. Appl. Crystallogr. 32 (1999) 379–380.
[14] A.A. Coelho, J. Evans, I. Evans, A. Kern, S. Parsons, The TOPAS symbolic computation system, Powder Diffr. 26 (2011), https://doi.org/10.1154/1.3661087. S22–S25.
[15] A. Belsky, M. Hellenbrandt, V.L. Karen, P. Luksch, New developments in the Inorganic Crystal Structure Database (ICSD): accessibility in support of materials research and design, Acta Crystallogr. Sect. B Struct. Sci. 58 (2002) 364–369, https://doi.org/10.1107/S0108768102006948.
[16] B.V. Chowdari, G.V. Subba Rao, G.Y. Lee, XPS and ionic conductivity studies on Li2O–Al2O3–(TiO2 or GeO2)–P2O5 glass–ceramics, Solid State Ion. 136–137 (2000) 1067–1075, https://doi.org/10.1016/S0167-2738(00)00500-2.
[17] M.L.F. Nascimento, L.A. Souza, E.B. Ferreira, E.D. Zanotto, Can glass stability parameters infer glass forming ability? J. Non-Cryst. Solids 351 (2005) 3296–3308, https://doi.org/10.1016/j.jnoncrysol.2005.08.013.
[18] A. Kiani, L.S. Cahill, E.A. Abou Neel, J.V. Hanna, M.E. Smith, J.C. Knowles, Physical properties and MAS-NMR studies of titanium phosphate-based glasses, Mater. Chem. Phys. 120 (2010) 68–74, https://doi.org/10.1016/j.matchemphys.2009.10.023.
[19] C.R. Mariappan, G. Govindaraj, Conductivity and ion dynamic studies in the Na4.7+xTi1.3-x(PO4)3.3-x ($0 \leq x \leq 0.6$) NASICON material, Solid State Ion. 176 (2005) 1311–1318, https://doi.org/10.1016/j.ssi.2004.12.013.
[20] H. Bradtmüller, A.M. Nieto-Muñoz, J.F. Ortiz-Mosquera, A.C.M. Rodrigues, H. Eckert, Glass-to-crystal transition in the NASICON glass-ceramic system Na1+xAlxM2−x(PO4)3 (M=Ge, Ti), J. Non-Cryst. Solids 489 (2018) 91–101, https://doi.org/10.1016/j.jnoncrysol.2017.10.057.
[21] C. Delmas, A. Nadiri, J.L. Soubeyroux, The NASICON-type titanium phosphates ATi2(PO4)3 (A=Li, Na) as electrode materials, Solid State Ion. 28–30 (1988) 419–423, https://doi.org/10.1016/S0167-2738(88)80075-4.
[22] D. Wang, Q. Liu, C. Chen, M. Li, X. Meng, X. Bie, Y. Wei, Y. Huang, F. Du, C. Wang, G. Chen, NASICON-structured NaTi2(PO4)3@C nanocomposite as the low operation-voltage anode material for high-performance sodium-ion batteries, ACS Appl. Mater. Interfaces 8 (2016) 2238–2246, https://doi.org/10.1021/acsami.5b11003.
[23] C.T. Moynihan, D.L. Gavin, R. Syed, Pre-exponential term in the Arrhenius equation for electrical conductivity of glass, J. Phys. Colloq. 43 (1982), https://doi.org/10.1051/jphyscol:1982975. C9-395-C9-398.
[24] J.L. Souquet, Ionic transport in glassy and polymer electrolytes, in: Defects Disord. Cryst. Amorph. Solids, Springer Netherlands, Dordrecht, 1994, pp. 221–244, https://doi.org/10.1007/978-94-011-1942-9_10.
[25] L. Zhang, H. Eckert, Short- and medium-range order in sodium aluminophosphate glasses: new insights from high-resolution dipolar solid-state NMR spectroscopy, J. Phys. Chem. B 110 (2006) 8946–8958, https://doi.org/10.1021/jp060501s.
[26] M. Neyret, M. Lenoir, A. Grandjean, N. Massoni, B. Penelon, M. Malki, Ionic transport of alkali in borosilicate glass. Role of alkali nature on glass structure and on ionic conductivity at the glassy state, J. Non-Cryst. Solids 410 (2015) 74–81, https://doi.org/10.1016/j.jnoncrysol.2014.12.002.
[27] L. Maia, A.C.M. Rodrigues, Electrical conductivity and relaxation frequency of lithium borosilicate glasses, Solid State Ion. 168 (2004) 87–92, https://doi.org/10.1016/j.ssi.2004.02.016.
[28] J.C.C. Abrantes, J.A. Labrincha, J.R. Frade, Applicability of the brick layer model to describe the grain boundary properties of strontium titanate ceramics, J. Eur. Ceram. Soc. 20 (2000) 1603–1609, https://doi.org/10.1016/S0955-2219(00)00022-4.
[29] I.M. Hodge, M.D. Ingram, A.R. West, Impedance and modulus spectroscopy of polycrystalline solid electrolytes, J. Electroanal. Chem. Interfacial Electrochem. 74 (1976) 125–143, https://doi.org/10.1016/S0022-0728(76)80229-X.
[30] J.T.S. Irvine, D.C. Sinclair, A.R. West, Electroceramics: characterization by impedance spectroscopy, Adv. Mater. 2 (1990) 132–138, https://doi.org/10.1002/adma.19900020304.
[31] R. Schmidt, J. Wu, C. Leighton, I. Terry, Dielectric Response to the Low-Temperature Magnetic Defect Structure and Spin State Transition in Polycrystalline LaCoO3, vol 79, 2009, pp. 1–8, https://doi.org/10.1103/PhysRevB.79.125105.
[32] P. Maldonado-Manso, E.R. Losilla, M. Martínez-Lara, M.A.G. Aranda, S. Bruque, F.E. Mouahid, M. Zahir, High lithium ionic conductivity in the Li1+xAlxGeyTi2-x-y(PO4)3 NASICON series, Chem. Mater. 15 (2003) 1879–1885, https://doi.org/10.1021/cm021717j.
[33] H. Randriamahazaka, K. Asaka, Electromechanical analysis by means of complex capacitance of bucky-gel actuators based on single-walled carbon nanotubes and an ionic liquid, J. Phys. Chem. C 114 (2010) 17982–17988, https://doi.org/10.1021/jp106232s.

Please cite this article as: A.M. Nieto-Muñoz et al., The role of Al^{+3} on the microstructural and electrical properties of $Na_{1+x}Al_xTi_{2-x}(PO_4)_3$ NASICON glass-ceramics, Journal of Alloys and Compounds, https://doi.org/10.1016/j.jallcom.2019.153148